Discover Sensors

RESEARCH Open Access

3D-printed split ring resonators as potential microwave strain sensors

Z. Viskadourakis[1*], M. Orfanou[2], A. Theodosi[1,3], O. Tsilipakos[4], E. Koudoumas[2,5] and G. Kenanakis[1*]

*Correspondence:
Z. Viskadourakis
zach@iesl.forth.gr
G. Kenanakis
gkenanak@iesl.forth.gr
[1]Institute of Electronic Structure and Laser, Foundation for Research and Technology-Hellas, N. Plastira 100, 70013 Heraklion, Greece
[2]Department of Electrical and Computer Engineering, Hellenic Mediterranean University, Estavromenos, 71004 Heraklion, Greece
[3]Department of Materials Science and Engineering, University of Crete, 70013 Heraklion, Greece
[4]Theoretical and Physical Chemistry Institute, National Hellenic Research Foundation, 11635 Athens, Greece
[5]National Institute for R&D in Microtechnologies-IMT Bucharest, 077190 Bucharest, Romania

Abstract

In the current study, mm-scale, split ring resonator meta-atoms are tested as potential strain sensors. In particular highly flexible, stand-alone split ring resonators were developed employing the so-called stereolithography technique, and subsequently coated with conductive silver paste, to achieve high electrical conductivity. All of them, exhibit sizable resonance features in the frequency regime 3–8 GHz, depending on their dimensionality. In order to study their electromagnetic response upon strain deformations, meta-atoms were attached on highly flexible stripes, made of acrylic joint sealant. In all cases, a clear shift of the linear electromagnetic response was recorded, upon strain induced (up to 40%), enabling their sensing capability. Such experimental results were further confirmed by corresponding theoretical simulations. The performance of such strain sensors was evaluated through strain sensitivity and strain gauge factor, reaching up to 6.1 MHz/%, and 0.144 respectively. On the other hand, the electromagnetic performance of the SRRs, in the presence of strain, was verified through the quality factor, laying in the range 40–50, while the measurement error was found to be 2.3–14%, depending on the sample. Moreover, all resonators exhibited high durability in fatigue experiments, as well as they did not show any hysteretic behavior, upon a full stress-destress cycle. Thus, 3D—printed split ring resonator metasurfaces emerge as potential candidates for strain sensing applications.

1 Introduction

Microwave resonating strain sensors are devices, the resonating frequency (laying in the range of GHz) of which is shifted upon force loading [1, 2]. Considering their type they can be categorized in microstrip resonators [3], interdigital capacitors [4], and split ring resonators [5, 6]. Compared to conventional resistive and capacitive strain counterparts, microwave resonator strain sensors exhibit distinct advantages, such as they are highly sensitive, accurate, low cost, miniature sized and they can perform in harsh environments. Furthermore, they can perform non-contact measurements, they can give feedback in real-time, through distant points. Therefore, resonant strain sensors become attractive for the detection of strain forces in civil engineering structures [7], in aerospace [8], in wearable devices [9], to name but a few.

Among the other resonant strain sensor types, the split ring resonator (SRR) sensor, is a metamaterial-based structure [10] consisting of a metallic loop, which is interrupted by a gap that breaks electrical continuity. From electronics' point of view an SRR can be viewed as a resonant RLC circuit, with effective resistance and inductance coming from the metallic loop, while the gap introduces an effective capacitance [5]. Each ideal RLC circuit exhibits a resonance frequency, given by the relation $= 1/2\pi\sqrt{LC}$. Therefore, the resonance frequency is affected by both the inductance and the capacitance of the circuit. In SRRs, the effective capacitance is correlated to the gap, while effective inductance is directly correlated to the dimensions of the SRR. Therefore, by carefully tuning either the shape or the dimensions of the SRR, i.e. by stretching or compressing it, shape deformation occurs, inducing observable shift in the resonance frequency. Hence, the detection of mechanical strains can be obtained through the monitoring of the SRR electromagnetic (EM) response, giving rise to the strain sensing capability of the SRR. Compared to the traditional resistive/capacitive gauges, SRR strain sensors are quite efficient, since they exhibit high sensitivity, excellent resolution and precision, quick response, and endurance in harsh environments as all microwave strain sensors. Moreover, they are wireless, thus they can be remotely operated, they do not consume power, thus no batteries are need. Even more they can be appropriately designed to perform in specific frequency ranges, i.e. taking in advantage of the cell phone networks for their stimulation / feedback, providing with crucial information in real-time. All the aforementioned advantages make SSRs very attractive alternatives for strain sensing. Up to date, SRR-based strain sensors have been developed, for numerous applications including the structural health monitoring [11, 12], aerospace [13, 14], biomedical applications [15–17] wearable devices [18–21], etc.

In addition, microwave SRR strain sensors get even more interesting, since, since they can be developed employing novel growth technologies, such as additive manufacturing [22, 23]. Indeed, 3D printing technology enables the capability to produce complex SRR meta-atoms, with very precise dimensions. Moreover, 3D printing technology allows the easy, quick and massive production of SRRs, using ordinary, eco-friendly materials. In such way the overall cost is reduced, industry – scale production can be achieved, while safe environmental conditions can be kept. Hence the development of microwave SRR structures, employing 3D printing technology, is gathering great interest for sensing applications.

Despite the great number of studies in microwave strain sensors [16–18, 21, 24–26] (and their references), up to now there are quite limited reports on 3D printed SRR-based strain structures [27–30]. Even more, in all those cases the strain sensor is grown on a flexible substrate, thus any possible separation between substrate and the sensor is forbidden. To the best of our knowledge there is no report on the 3D development of stand-alone SRR-based sensors, which can be mounted to any stretchable surface. Considering the above, we hereby study the capability of single rectangular SRRs, as strain sensors. The SRRs have been grown, employing the so—called stereolithography method. The proposed SRR geometry is simple, but well—studied in the literature, although it could support strong and sharp resonance phenomena, which is beneficial in sensing applications. On the other hand, the SRR developing method is a well-established and straight-forward additive manufacturing procedure. In addition, commercially available stereolithography printers, exhibit printing resolution in the

range of 10–100 μm, depending on the printing material. Such printing resolution is quite enough for mm-scale structures. Furthermore, the whole procedure is quick, easy to the user, eco-friendly, and mass productive, since multiple SRRs can be grown at the same time, even though the procedure takes place into a research lab. Considering the above, both the morphology and growth method enable the SRR's quick, low cost, large-scale production, without sacrificing its potential detection efficiency.

All produced SRRs were characterized with respect to their EM behaviour. All of them respond in the frequency range 3–8 GHz, depending on their dimensions. In order to examine their sensing capability with respect to strain, SRRs were being attached to properly grown stripes made by acrylic joint sealant paste, a material exhibiting very high flexibility. By stretching the sealant stripe, the SRR shape changes giving rise to resonance frequency shifts. In such way, the SRR detects strain forces applied. Combined tensile test and EM response experiments were performed, in order to record such behaviour. The experimental results show a sizable blue shift in the resonance frequency upon strain, along with an enhancement of the transmission magnitude, for all studied SRRs, for strains up to 40%. Corresponding theoretical simulation results corroborate the experimental evidence, verifying the strain capability of the proposed SRR sensors. Moreover, the studied SRRs show very good flexibility behaviour, since they fully recover (regarding their shape) after each stress-release cycle, without any hysteresis in their EM performance. Furthermore, they also exhibit a rigid endurance in multiple consecutive stress-release cycles, without showing any significant degradation of their EM performance. Hence, the 3D printed SRR meta-atoms emerge as novel and promising alternatives for applications in strain sensing.

2 Experimental details

2.1 Split ring resonator fabrication

Rectangular SRRs have been fabricated employing the so-called stereolithography (SLA) method. In the SLA method, a light source cures a liquid resin into hardened plastic. A commercially available FormLabs Form 3 + (Formlabs, MA, USA) printer is used along with the Formlabs Black Resin V2, as starting material. "Default printing parameters" and "0.100 mm layer thickness" were chosen in the PreForm software, which is the dedicated software for printer operation. In addition, for optimal printing results, the "Auto-generate support" tool was used to develop the structures in an appropriately grown support web, during the printing process. After finishing the printing process, all structures were ultrasonically treated in isopropyl alcohol, for 20 min. Following the above-described procedure, SRRs of several dimensions were fabricated, as shown in Fig. 1a. Corresponding dimensions are listed in Table 1. After their construction, all SRRs are coated with conductive silver paste (coating thickness ~ 0.1 mm). Such a procedure has been successfully used in previous studies, so as the meta-atoms become conductive, allowing to support strong conduction currents and leading to well-defined resonances [31–33].

2.2 Joint sealant stripe fabrication

Stripes of acrylic joint sealant were prepared, as follows: At first the sealant was rolled out onto a greaseproof paper using a spatula, so that a thick sheet is formed. The sealant sheet was left to dry overnight. Then it was removed from the paper and a pasta machine

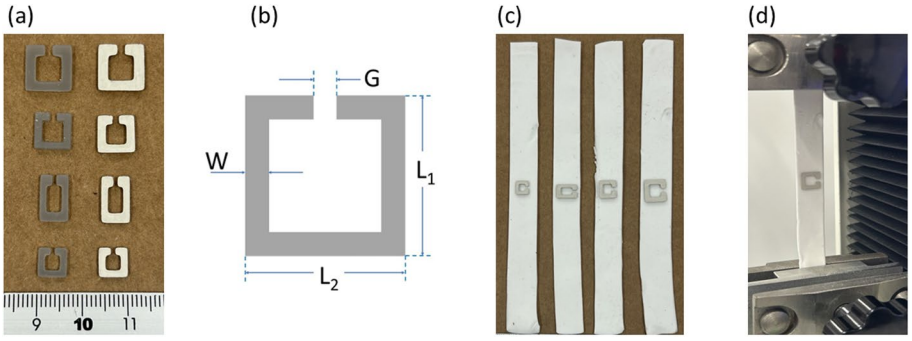

Fig. 1 **a** SLA printed SRRs, of various dimensions, bare (left column) and coated with silver paint. (right column). **b** SRR dimensions. **c** Sealant stripes with SRRs attached at the center of them. The SRR gap is placed parallel to the stripe long direction. **d** Stripe/SRR placed on the tensile test machine

Table 1 Sample codes, corresponding dimensions and electromagnetic characteristics of all stand-alone SRRs

Code	L_1 (mm)	L_2 (mm)	W (mm)	G (mm)	f_r (GHz)	$S_{21,\,max}$ (dB)
S1	10.17 ± 0.05	10.16 ± 0.05	2.19 ± 0.08	1.72 ± 0.07	4.83	−15.71
S2	8.13 ± 0.06	8.1 ± 0.1	1.76 ± 0.08	1.44 ± 0.08	5.90	−11.03
S3	6.48 ± 0.05	6.35 ± 0.06	1.53 ± 0.07	1.0 ± 0.2	7.78	−8.10
S4	10.23 ± 0.05	6.24 ± 0.05	1.7 ± 0.2	1.0 ± 0.2	5.95	−11.61

was used in order to reduce the thickness of the sheet, down to ~ 2 mm. After that, long and narrow stripes of joint sealant were extracted. Typical dimensions of each stripe are 150 mm × 20 mm × 2 mm (Fig. 1b).

2.3 Stripe—SRR assembly

After sealant stripe fabrication, stripes with SRRs attached on their surface were prepared. More specifically, an SRR was glued at the center of each stripe. The orientation of the SRR is such that the gap is parallel to the stripe length (Fig. 1c). Notably, only the edges of the SRR gap were glued onto the stripe, thus the rest of the SRR body can be freely deformed, following any deformation of the stripe, due to the application of strain. Thus, by stretching the stripe, the SRR gap can widen (capacitance decreases), leading to an increase of the resonance frequency.

2.4 Mechanical properties characterization

The tensile properties of joint sealant stripes were examined, using a universal test machine (BIOBASE BKWW-5S, Shandong, China). Each stripe is appropriately wrapped in the machine clamps, which move away from each other at a constant velocity of 1 mm/sec (Fig. 1d). During the entire procedure, the elongation ΔL of the stripe and the loaded force F are simultaneously recorded. Then the tensile stress is calculated through the relation $P = F/A$, where A is the cross section of the stripe. Additionally, tensile strain is calculated by the relation $\Delta L/L_o$ (%), where L_o is the initial length of the sample (equals to the length between the test machine clamps). Corresponding tensile strength—strain curves are extracted from these experiments (i.e., see supplementary Figure S1).

2.5 Electromagnetic characterization

The EM behavior of all stand-alone SRRs was determined through transmission experiments, in the frequency range 3–10 GHz. For those experiments, an appropriate experimental set-up was used, consisting of a Keysight P9372B Vector Network Analyzer (Keysight, California, USA) in combination with WR187 (frequency range 3.5–7 GHz) and WR137 (frequency range 5–10 GHz) waveguides (depending on the SRR dimensions). SRRs attached on small pieces of sealant stripes were placed in the middle of the waveguide and transmission spectra were collected, by recording the S_{21} parameter, with respect to the frequency. The SRR was oriented in such a way inside the waveguide so that the gap is parallel to the y axis, in order to allow excitation by the fundamental TE_{10} mode (Fig. 2a).

2.6 Combined tensile stress–strain/electromagnetic response experiments

After verifying the EM behaviour of the developed SRRs, further experiments were performed, in order to correlate the EM response of the meta-atoms to the tensile properties of the sealant stripes. In this context we employ a modified experimental set-up, initially proposed by Melik et al. [34], in which the tensile stress of the joint sealant stripe and the EM response of the attached SRR could be recorded, simultaneously, as shown in Fig. 2b. More specifically, the hereby set-up is described as follows: two waveguide segments are joined, but a narrow opening (3.5 mm) is left between them by using metallic spacers. Through this narrow opening, the joint sealant stripe, with the SRR attached, can be inserted, and its ends are fixed in the tensile test machine clamps (Fig. 1d). The SRR is appropriately placed in the middle of the waveguide, thus enabling EM measurements with minimal interruption of the waveguide environment. Naturally, the opening in the waveguide will introduce some parasitic background effects in the measurement, i.e. frequency shift towards lower values. Such a shift directly depends on the opening width, as well as the SRR dimensions. Thus, the opening width is kept constant (3.5 mm), slightly larger than the width of the samples under test, so that the waveguide induced frequency shift will be reproducible, each time that the same SRR is measured, warranting the high accuracy of the measurement. Nonetheless, as it will be presented

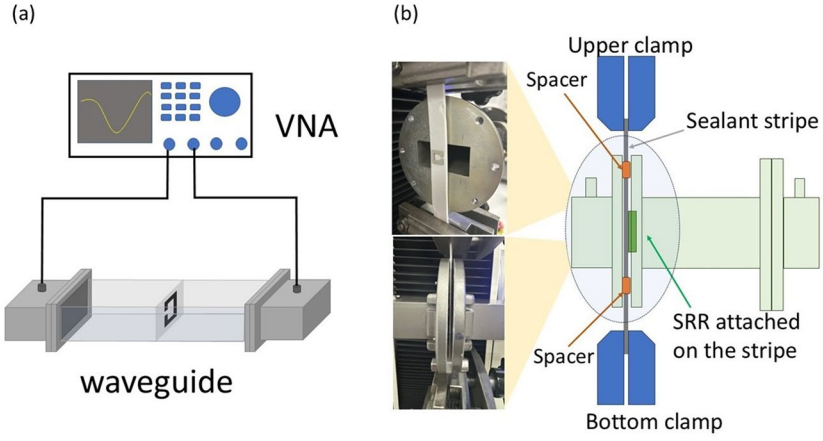

Fig. 2 **a** Set-up for electromagnetic measurements. The orientation of the sealant stripe into the waveguide is clearly presented. **b** Experimental set-up for combined tensile—electromagnetic measurements. The exact position of the sealant stripe with the attached SRR is clearly shown in the left upper photograph. The narrow opening is also seen in the left bottom inset, through which the sealant stripe is inserted

below, the EM signal coming from the SRR is strong enough, keeping a high signal to noise ratio. The stripe was stretched, with a low but constant speed (0.5 mm/sec), while both the stretching force and the S_{21} vs. f spectra are simultaneously recorded, Therefore, the tensile properties of the stripe along with the EM behaviour of the SRR can be investigated at the same time.

Using this experimental set-up, various experiments were performed. At first the EM response of each SRR was recorded with respect to the tensile force, in order to determine the correlation between the typical tensile stress – strain curve, with the EM behaviour of the SRR. Moreover, hysteresis experiments were performed. More specifically, each sealant stripe was subjected to a desired tensile force and the corresponding EM response of the attached SRR was recorded. This procedure was repeated as the tensile force was increased in distinct steps, up to a final value. Then the same procedure was followed, while decreasing strain, in steps, until the sample was fully released. Finally, fatigue experiments were performed, in which the stripe was continuously stretched and released, within the elastic deformation regime, while EM spectra were collected in each state. The experiment was repeated several hundreds of times, in order to study any EM degradation of the SRR performance, due to stress-release cycles.

Here it has to be noted that, the proposed experiments were being occurred in laboratory conditions, where temperature is controlled (25 ± 2 °C). At such temperature the acrylic joint sealant does not changing its behaviour and possesses minimized thermal-induced changes (in general, acrylic sealants are considered as efficient materials for general construction joints, minor movement joints, and gaps where high elasticity and adhesion are required). Moreover, the proposed SRR topology and its variations are less sensitive to temperature but remain highly responsive to mechanical strain [35]. As a result, the proposed SRRs' topology (e.g., gap size, ring width) is properly selected so that any temperature effects barely affect its electromagnetic behaviour. In addition, the proposed, modified experimental set-up is dedicated for laboratory experiments, where several crucial experimental parameters can be gently manipulated, towards the optimization of the experiment. In real-world applications, it may not be that effective, since sensors generally will be affected by factors that cannot be manipulated. Therefore their operation and performance will be rather different than inside a waveguide. In such case the use of horn antennas, would be more effective.

2.7 Theoretical simulations

Prior to the experimental procedure, rigorous Finite Element Method (FEM) simulations were employed to clarify that the proposed SRRS could function as a strain sensor. Solid mechanic and electromagnetic simulations were conducted using the commercial software COMSOL Multiphysics, which implements the Finite Element Method. First, the SRRs were electromagnetically modeled in the absence of strain. Subsequently, the complete geometry of silver-painted SRRs on sealant stripes was subjected to tensile stress, matching the magnitude applied in the experiment. The resulting deformed geometry was then studied again electromagnetically to determine the frequency shift caused by this deformation.

For the mechanical properties of materials, the joint sealant stripes were modeled as a hyperelastic material with rubber-like behavior. This material was assumed to have Mooney-Rivlin parameters $C_{10} = 0.37$ MPa and $C_{01} = 0.11$ MPa. The bulk modulus was

$\kappa = 10^4$ MPa and the density $\rho = 1500$ kg/m^3. The polymeric material of the SRRs was modelled as a Neo-Hookean material with Lame parameter $\mu = 0.2 \times 10^9$ N/m^2, bulk modulus $\kappa = 10$ GPa and density $\rho = 1145$ kg/m^3. The viscoelasticity of the polymer was described using a Kelvin-Voight model with relaxation time equal to $\tau_v = 3000$ s. Finally, silver was modelled as an isotropic linear elastic material with Young's modulus E = 70GPa, Poisson's ratio $\nu = 0.37$ and density $\rho = 10500$ kg/m^3. In the mechanical simulations, one end of the sealant stripe was fixed (zero displacement) to prevent rigid body motion, while a tensile load was applied to the opposite end to induce deformation.

The full-wave electromagnetic simulations were performed using the frequency domain solver with a continuous-wave (CW) excitation. The stripe was placed in the center of a WR187 waveguide with dimensions 47.5 mm × 22.1 mm. The waveguide walls were modeled as boundary conditions of a perfect electric conductor (PEC). This type of boundary condition sets the tangential component of the electric field to zero. The TE_{10} mode of the waveguide was used to excite the structure and the S-parameters were calculated by using the built-in rectangular waveguide ports. Both SRR polymer and sealant stripe were modelled via their dispersionless relative electric permittivity which was considered to be 3–0.03i (loss tangent of 0.01). Finally, the silver paste coating was modelled via the electric conductivity of 10^5 S/m. Typical simulation results for the S1 sample are shown in Supplementary Figure S2.

3 Results and discussion

Figure 3a shows the EM behavior of all stand-alone SRRs. All of them exhibit a well-defined drop in the S_{21} curve at certain frequencies, associated with the excitation of the SRR resonance. The corresponding resonant frequencies f_r and transmission dips (minimum S_{21} magnitude) are compiled in Table 1; the observed values are in good agreement with others previously reported for 3D printed SRRs, of similar dimensions [31]. In addition, it is also seen that the resonance frequency increases with decreasing SRR dimensions, as anticipated. When attached to sealant stripe, the EM behavior of the SRR is affected, i.e., the resonance frequency shifts towards lower values (Fig. 3b). This is due to the dielectric permittivity of the acrylic sealant stripe ($\varepsilon' \sim 3$) [36], which is greater than that of air ($\varepsilon' = 1$). Further shift of the resonance frequency is observed when the sealant stripe, with the SRR attached, is placed to the experimental set-up, dedicated for tensile stress/EM measurements (blue line, Fig. 3b). This further reduction is attributed to the

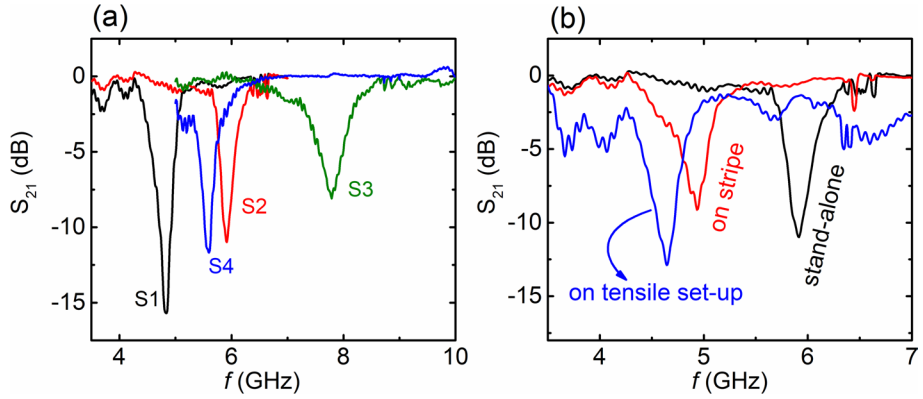

Fig. 3 **a** S_{21} vs frequency curves for all studied SRRs. **b** S_{21} vs frequency curves for S2 sample as stand-alone (black line), attached to the joint sealant stripe (red line) and when it is placed in the tensile/EM set-up (blue line)

perturbation of the mode guided in the waveguide, due to the opening. However, there is not any change observed in the S_{21} curvature, while no other significant changes in the S_{21} spectrum are shown. Similar trends are observed for all studied SRRs.

Finally, all studied SRRs exhibit resonating features in the frequency regime 3–8 GHz, enabling their potential operation in 5G band [37], which is established for wireless communications, throughout the world. The proposed SRRs can be appropriately designed, regarding their dimensions, so that they exhibit their optimal performance in frequencies within the 5G band. Therefore, they can be stimulated by existing communication networks, without needed any further instrumentation. Even more they can be probed by the same networks, giving back strain data, remotely, in real time, without needing any measurement instrument. Hence the performance of the proposed SRRs in to 5G environments can be beneficial, regarding their potential uses.

Figure 4a shows the EM response of the S2 sample with respect to the strain, loaded to the joint sealant stripe. A well-defined S_{21} dip is observed at ~ 4.64 GHz, due to the

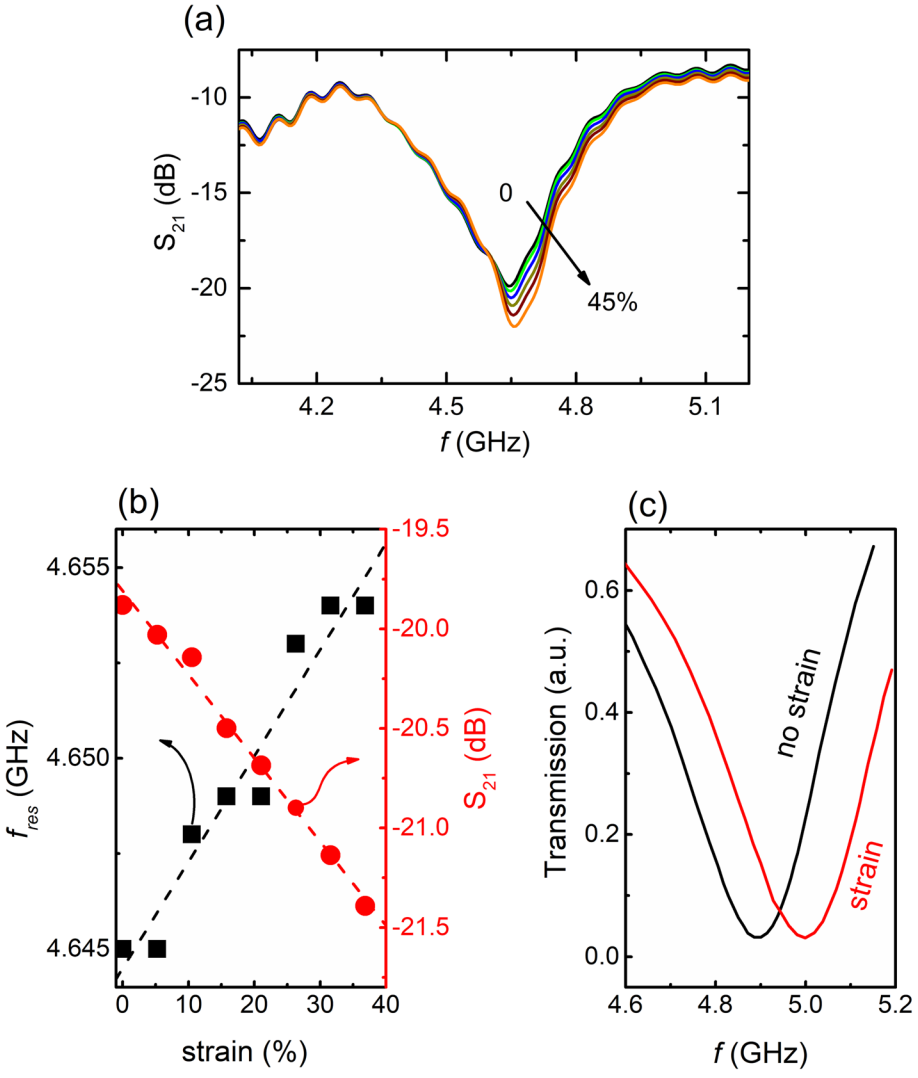

Fig. 4 **a** S_{21} vs. f curves for the S2 SRR upon various strains. Corresponding **b** f_{res} vs strain and (black line and symbols) and S_{21} vs. strain graphs (red line and symbols) as extracted from panel (**a**). Dashed lines correspond to linear fits as described in the main text. For all linear fits $R^2 > 0.99$. **c** Theoretical simulation results for S2 sample, upon 20% strain

resonance at this frequency (black curve). Interestingly, upon the application of strain in the sealant stripe, the drop is shifted to higher frequencies, while it becomes more pronounced. Thus, the detection of the applied strain, through the EM response of the SRR can be realized. Corresponding theoretical simulations clearly show a blue shift in the resonance, upon strain (Fig. 4c for S2 sample; supplementary Figure S3 for all studied SRRs), corroborating the experimental evidence. Here it must be noted that the application of strain widens the SRR gap. It has been previously observed that for rectangular 3D printed SRRs, the larger the gap, the higher the resonance frequency [31], as anticipated due to the reduction in capacitance. The resonance shift, as well as the corresponding S_{21} magnitude are plotted with respect to the strain, as shown in Fig. 4b.. Both the resonant shift and the S_{21} magnitude depend linearly on the strain, which is anticipated for small capacitance changes/frequency shifts. Qualitatively, the linear dependence of the resonance frequency, has been shown for other SRR sensors as well [34, 38–40], coinciding the hereby results. The evolution of the EM response of the SRR, with respect to the strain, extends for strains up to 40%, highlighting the high flexibility of the studied SRRs, which mainly is attributed their polymer-based core. Such high flexibility could be beneficial, since these strain sensors can potentially conform to wavy surfaces, and probe their slight deformations. Notably, similar results are obtained for all studied SRRs (i.e., see supplementary Figs. S4 to S6).

Further analysis in the data of Fig. 4b, reveals that the resonance frequency can be fitted through the linear model $f_{res} = f_o + A \cdot \frac{\Delta L}{L_o}$, where f_{res} is the resonance frequency upon strain, f_{o} is the resonance frequency under no strain and $\Delta L/L_o$ is the strain induced to the stripe. Such a linear equation can be transformed to:

$$A = \frac{f_{res} - f_o}{\Delta L/L_o} = \frac{\Delta f}{\Delta L/L_o} = S_f \tag{1}$$

where S_f is defined as sensitivity of the SRR-based strain sensor and sufficiently describes its performance. Thus, the sensitivity S_f can be calculated through the slope of the f_{res} vs. strain graph (black dash line, Fig. 4b). Corresponding results for all samples, are listed in Table 2 (experimental data and appropriate linear regressions, for samples S1, S3 and S4, are shown in supplementary Figs S4, S5 and S6, respectively). By comparing the frequency slopes, the S4 sample shows the largest slope value, clearly indicating the higher sensitivity of all. Following similar analysis for the S_{21} data (red circles, and dash line, Fig. 4b), sensitivity can also be determined through S_{21} vs. strain graph, i.e., $S_{S_{21}} = \Delta S_{21}/(\Delta L/L_o)$). Thus, by comparing the S_{21} slope, the S1 sample shows the highest slope value. Considering the above, strain sensor sensitivity could be determined through both the resonant frequency and the S_{21} magnitude, although there is not any clear indication which SRR is the most sensitive, in our case. To clarify such a discrepancy, we calculated the gauge factor GF [38, 39]:

Table 2 Calculated strain performance coefficients for all studied samples

Sample	S_f (MHz/%)	$S_{S_{21}}$ (dB/%)	GF
S1	2.5 ± 0.2	0.39 ± 0.01	0.063 ± 0.003
S2	0.28 ± 0.03	0.042 ± 0.002	0.0059 ± 0.0006
S3	2.6 ± 0.1	0.19 ± 0.02	0.037 ± 0.002
S4	6.1 ± 0.1	0.18 ± 0.03	0.144 ± 0.004

$$GF = \frac{|f_{strain} - f_o|}{f_o \cdot \frac{\Delta L}{L_o}} \tag{2}$$

where f_o is the resonance frequency of unstrained SRR, f_{strain} is the resonance frequency of SRR, upon strain. In this context, the appropriate frequency shift $\Delta f / f_o$ as a function of strain is shown in Fig. 5, for all studied samples. The linear response of the frequency shift, with respect to the strain is clear for all samples (dashed lines), the accuracy of which has been determined through the coefficient of determination (R-squared), $R^2 > 0.99$, for all samples. The slope of each curve corresponds to the GF value, which is presented in Table 2. Considering both the sensitivity and the GF it comes out that S4 sample seems to perform better as strain sensor, compared to the others.

From the EM point of view, the sensing performance of studied SRRs be quantified through the the quality factor *Q*, relative sensitivity *S(%)*, and the Figure of Merit *FoM*, through the following relations:

$$Q = \frac{f_o}{FWHM} \tag{3}$$

$$S\,(\%) = 100 \times \frac{f_{strain} - f_o}{f_o \cdot \left(\varepsilon'_{stripe} - \varepsilon'_z\right)} \tag{4}$$

$$FoM = \frac{S}{FWHM} \tag{5}$$

where f_o is the resonance frequency, for each unstrained sample on the stripe, *FWHM* is the full width at half maximum of each transmission minimum, f_{strain} is the resonance

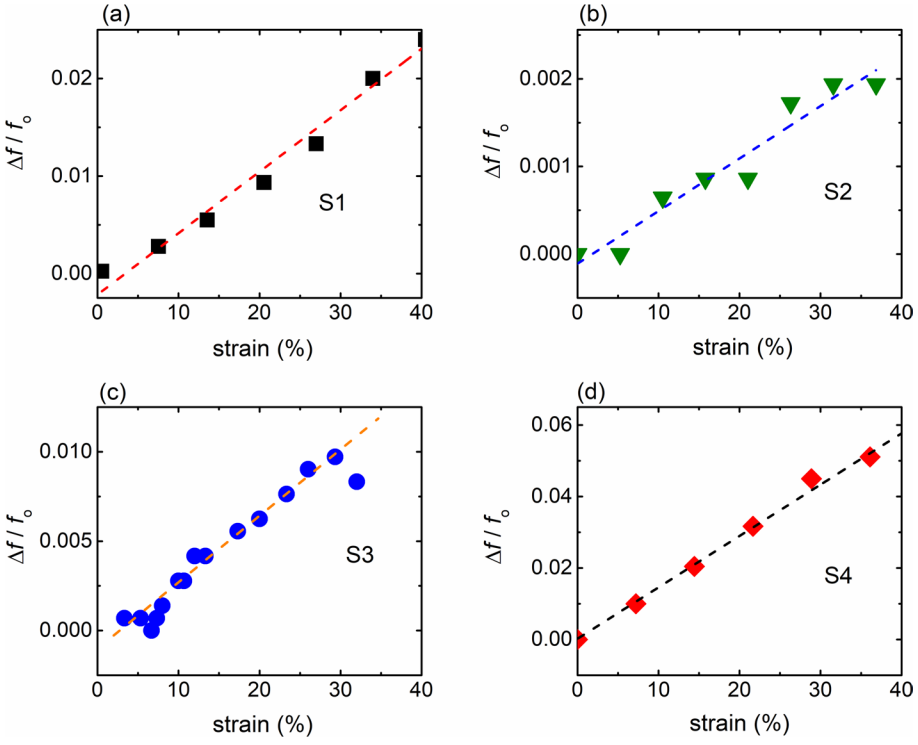

Fig. 5 $\Delta f/f_o$ vs. strain curves for **a** sample S1, **b** sample S2 **c** sample S3 and **d** sample S4. Dash line are linear fits as described in the main text. For all linear fits $R^2 > 0.99$

frequency of each SRR upon strain, ε'_{stripe} is the dielectric permittivity of the stripe under 1% strain, while ε'_z is the corresponding dielectric permittivity of the stripe under no strain. It is useful to notice that the sensitivity *S(%)* is different than the sensitivity S_f, presented in Table 2. The former corresponds to the performance of the SRR as an electromagnetic device, while the latter refers to the evaluation of the SRR-based strain sensor efficiency. In addition, it should be noted that dielectric permittivity is affected by the strain. In general, it has been previously shown that ε' tends to decrease with increasing strain, for elastomer materials [41–43]. Moreover ε' also depends on the stretching speed [41]. For elastomers, such as the acrylic joint sealant used in this study, typical dielectric permittivity value $\varepsilon'_z \approx 3$, in the high frequency region [44, 45]. Such a value is estimated to be reduced by ~ 3%, for strain load of 1%, therefore $\varepsilon'_{stripe} \approx 2.9$ [41]. Assuming the above, the calculated quantities are presented in Table 3. Furthermore, in comparison to the simulation results, the performance error of the investigated SRRs, is calculated through the following formula:

$$Error\% = 100 \cdot \frac{|f_{meas} - f_{sim}|}{f_o} \tag{6}$$

where f_{meas} is the measured frequency upon a specific strain load, f_{sim} is the frequency upon a specific strain load, extracted from simulations, and f_o is the measured frequency, upon no strain. Corresponding values and performance errors are listed in Table 3.

It has to be noted that the $f_{strain} - f_o$ (relation (4)) is calculated for 1% strain increment, thus it is equal to the frequency slope, as shown in Table 2, for each SRR. From the above table it becomes clear that almost all SRRs show comparable *Q* factors, while S4 exhibits the largest *FoM* of all. Direct comparison among *FoM*, sensitivities and gauge factors (Table 2), it comes up that the EM response and the strain sensitivity of the studied SRRs are closely related. Therefore, an efficient SRR-based strain sensor should exhibit significant EM response. In addition, performance error values seem to be high, indicating a sizable difference between experimental and simulation results. However they are lower than other reported for microwave strain sensor [46]. Direct comparison between the studied SRR strain sensors and other resonator based sensors, is given in Table 4.

Comparing the sensitivities, it can be seen that the hereby SRR strain sensors, exhibit comparable or slightly better performance, against others reported so far [48, 49, 51–53]. Regarding GF, the hereby studied SRR strain sensors show comparable values with others reported so far [34, 38, 48, 57]. More interestingly, the proposed SRR sensors show a remarkably wide strain range (in which they efficiently respond), which reaches up to 40%, among the highest strain values presented in Table 4. Therefore, although their relatively average strain performance, the proposed SRR strains sensors exhibit a

Table 3 Calculated performance coefficients for all studied samples

Sample	f_o (GHz)	f_{strain}—f_o (MHz)	FWHM (GHz)	Q	S (%)	FoM	f_{meas} (GHz)	f_{sim} (GHz)	Error %(*)
S1	3.962	2.5 ± 0.2	0.082	48.2	0.66	8.0	4.00	3.80	5.1
S2	4.645	0.28 ± 0.03	0.240	19.5	0.056	0.23	4.65	4.99	7.5
S3	7.220	2.6 ± 0.1	0.116	47.5	0.36	3.1	7.25	7.46	2.9
S4	4.282	6.1 ± 0.1	0.152	28.2	1.42	9.4	4.40	5.00	14

*The performance error has been calculated, considering a 20% strain

Table 4 Performance of resonance based strain sensors, previously reported

References	S_f (MHz/%)	GF	f_o (GHz)	FWHM (GHz)	Q	Max. strain
[47]	0.87	2.24	40 M	23 M	1.7	< 5%
[48]	1.2	0.14	0.856	0.010	86	< 50%
[49]	0.5 dB/%	–	7.40	0.29	25.5	< 20%
[50]	3.45	–	3.79	0.256	14.8	*
[51]	6.5	0.041	31.3	1.5	21	–
[52]	6.5	–	8.67	0.3	29	< 5%
[53]	85	0.008	11.01	1.4	8.1	< 15%
[54]	12	–	5.2	0.023	226	–
[38]	16	0.42	3.64	0.29	13	< 115%
[39]	25	1.9	1.33	0.01	133	–
[55]	27	0.0042	5.341	0.047	114	< 0.3%
[56]	33	1.6	2.10	0.07	30	< 10%
[34]	52	0.42	12.3	0.16	13	< 5%
[57]	302	0.13	2.45	0.10	23	< 0.6%
[58]	1100	0.0014	797	113	7.0	< 5%
This work	6.1	0.144	4.28	0.152	28.2	> 40%

In [49] the sensitivity is determined through the S_{21} modulation

*bending strain sensors

sizable flexibility. Thus, the proposed SRR strain sensors exhibit sufficient strain sensing characteristics, towards a promising performance.

Improvement of the sensing capability, is closely related to the enhancement of the sensor's EM response. In general, efficient resonator sensors should show sharp S_{21} spectra, so that any tiny resonance shift would be detectable. In contrast, the broad minima exhibited in the hereby sensors' S_{21} spectra (Fig. 3), mainly contribute to the reduction of the overall SRR performance. Thus, the hereby SRRs' EM behavior could be optimized, towards their strain sensing performance enhancement. SRR EM response improvement, may be achieved through optimizing the development procedure of the SRR, the use of materials with higher electric conductivity, etc. On the other hand, the simple design of the proposed sensors, does not seem to be related to their reduced performance. Strain sensors, with simpler designs [40, 46, 49], exhibit significant sensing capabilities. Moreover, SRR-based strain sensors have also presented an effective performance [34, 55, 57]. Especially the proposed structure in [39], is almost similar to those studied here. All these sensors exhibit considerable strain characteristics, while their design is relatively simple. Thus, improvement of the hereby studied strain sensors' performance may be focused on the enhancement of their EM behavior rather than changing their design.

In their present state, the proposed SRR strain sensors exhibit adequate characteristics, to establish their potential capability as strain sensors. In the current investigation, it is evidently shown that, SRR strain sensors practically respond to strain changes, in a satisfactory level. Furthermore, their relatively low dimensions, their high flexibility and their simple, easy and quick construction, employing 3D printing technology, give to the proposed sensors further credence for potential uses. Of course there is a lot of space for further optimization, so that their performance could be boosted even more, reaching state-of-the-art, innovative shaped strain sensors. This is a main scope of a forthcoming investigation.

The EM response of the hereby SRRs as well as their performance as strain sensors are closely correlated as shown by the calculated sensitivities. Therefore, an effective

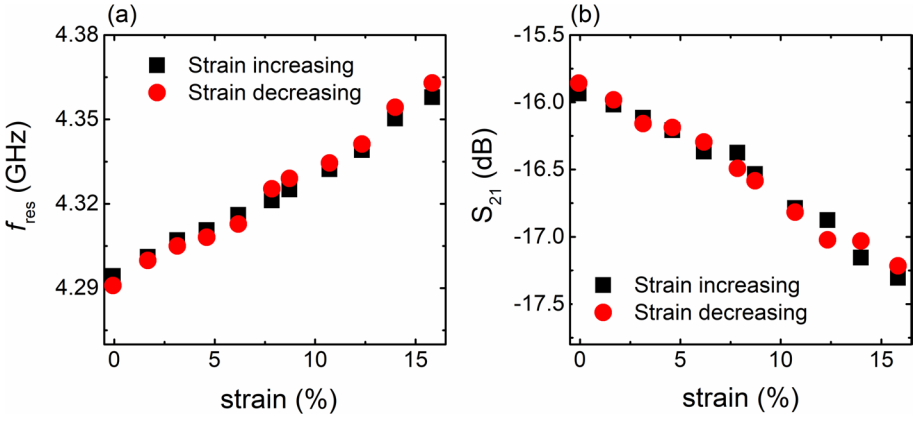

Fig. 6 **a** f_{res} vs. strain for S4 sample, upon increasing strain (black symbols) and decreasing strain (red symbols) **b** S_{21} magnitude as a function of strain upon increasing strain (black symbols) and decreasing strain (red symbols)

metasurface strain sensor, should exhibit distinctly high EM performance. To this end, we focus on the S4 sample, since it shows the most efficient performance of all. In order to confirm the intrinsic nature of the above observed strain-induced EM response, further experiments were conducted. In particular, the EM response of the SRR, was investigated, upon increasing and decreasing the strain applied to the sealant stripe, in order to record any possible hysteretic effects. Corresponding experimental results are shown in Fig. 6. It is obviously seen that resonance frequency (Fig. 6a) shows the same curvature in both ways, either when increasing or decreasing the strain, suggesting that there is not any hysteresis effect. Hence, in terms of sensing capability it is shown that SRRs identically respond upon strain forces. Notably similar behavior is observed for S_{21} magnitude as well (Fig. 6b).

Moreover, fatigue experiments were performed in order to study whether the SRR endurance sustains or not, upon the continuous use. Thus, sealant joint stripe is strained up to ~ 2% and then released, and this procedure continues for several hundreds of cycles. The frequency change is recorded every 10 cycles.

Experimental results, for S4 sample, are presented in Fig. 7. Two distinct frequency regions are observed (Fig. 7a), the low frequency regime, in which the SRR resonates when released, and the high frequency region, in which the SRR resonates, when in stress. It is clearly seen that, when stressed the resonance frequency of the metasurface increases, while upon release it returns to its initial value. Upon consecutive stress/release cycles the EM behavior of the metasurface keep uniform and reproducible, revealing an excellent retention character, upon continuous use. Therefore, SRRs not only show a significant response upon strain, but also they exhibit high endurance upon consecutive cycles of use. Such an observation could gain more interest, considering that the studied SRR sensors are covered with a thin silver paste coating in order to get high conductivity required for EM performance. Apparently, this coating probably does not exhibit as high flexibility as the polymeric core of the SRR, enhancing the probability for unwanted coating cracks, which could result in the SRR sensor failure. Nevertheless, the above described fatigue experiments evidently show that the silver paint coating persists in consecutive strain/release cycles, without any degradation in its conductivity performance, leading to the overall high endurance of the SRRs, making them very promising candidates for long-life, strain sensing applications.

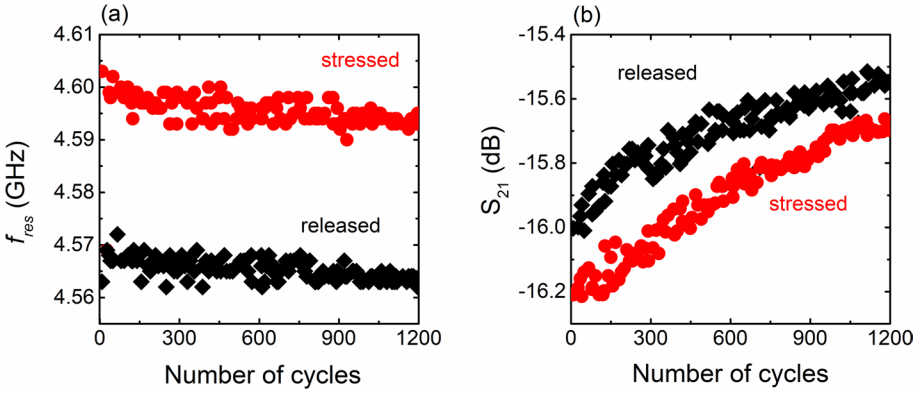

Fig. 7 **a** Resonance frequency with respect to the number of stress/release cycles for S4 sample. **b** S21 magnitude as a function of the number of consecutive stress/release cycles for S4 sample

In Fig. 7b S_{21} vs strain/release cycles, is shown. Similarly to Fig. 7a, two separate S_{21} areas are also seen, designating the two strain stages of the SRR. Nevertheless, the difference between them is not that obvious as in the case of the resonant frequency. In addition, the S_{21} magnitude decreases upon stress/strain cycles, indicating a relaxing behavior. Anyhow, S_{21} component, upon consecutive stress/release cycles seems to follow the response of the resonant frequency demonstrating the high endurance of the 3D printed SRR upon continuous mechanical stretching.

Finally, data presented in Fig. 7a, verify the reproducibility of the test and uniformity of the results. The average resonance frequency of the sensors in the stressed position is (4.595 ± 0.003) GHz (error has been calculated through standard deviation analysis). Such a result means that most of the measured frequencies (i.e., 68%) lay in a very narrow frequency band of ~ 6 MHz. Regarding the initial, non-strained state the average resonance frequency is (4.565 ± 0.002) GHz, while the most of the measured frequencies are localized in a ~ 4 MHz regime. Similar analysis can be made for the S_{21} data in Fig. 7b, from which it is comes out that the most of the S_{21} measured values are located within a ~ 0.2 dB band, regardless the strain state. Although the drifting behavior observed in Fig. 7b, experimental data seem to retain their uniformity.

4 Summary

In the current study rectangular SRRs were studied regarding their ability to act as strain sensors. The SRRs were grown using the stereolithography method and then they were coated with conductive silver paint, in order to achieve high electrical conductivity. The SRRs were characterized regarding their EM response, in order to confirm their resonance behavior in the regime 3–8 GHz, therefore the proposed SRR-based strain sensors could be incorporated to sensors' networks utilizing the 5G broadband.

After that they were attached to joint sealant stripes (a very flexible material) and combined stress–strain / transmission experiments were performed, so as the EM behavior of the SRRs was recorded with respect to applied strain. It was found that regardless the dimensions of the SRR its resonance frequency shifts to higher values with increasing strain, while the S_{21} magnitude decreases. Those experimental results were further confirmed by corresponding theoretical simulations. The frequency shift is linearly dependent on the strain, which enables the quantification of the strain through the SRR EM response. Moreover, SRRs exhibited a robust behavior when stressed—released several

times, without showing any performance degradation. Furthermore, they did not show any hysteretic behavior, upon strain, either in resonance frequency or in S_{21} magnitude. Therefore, 3D printed SRRs exhibit an efficient performance as strain sensors.

Corresponding strain sensing performance as well as EM efficiency factors calculated, were found to be comparable to others reported for resonance—based strain sensors. Thus, optimization of the current SRR sensors is needed in order to show even more efficient performance. Even though, these SRR strain sensors exhibit very high flexibility, which is combined with their strong and rigid EM modulation, upon strain application, establishing their capability and their potential use as strain sensors.

Supplementary Information

The online version contains supplementary material available at https://doi.org/10.1007/s44397-025-00019-9.

Supplementary material 1.

Author contributions

Z.V.: Conceptualization, methodology, data curation, supervision, writing / editing the original draft. O.T.: Investigation, data curation, validation, editing the original draft. M.O., A.T: Investigation, data curation, validation. E.K.: Validation, supervision G.K.: Conceptualization, investigation, project administration, funding.

Funding

This work was funded by the project "METAmaterial-based ENERGY autonomous systems (META-ENERGY; Project ID 2936)" which is implemented under the Second Call for H.F.R.I. "Research Projects to Support Faculty Members & Researchers" funded by the Operational Programme "Competitiveness, Entrepreneurship and Innovation" (NSRF 2014–2020).

Data availability

The datasets generated during and/or analyzed during the current study are available from the corresponding author on reasonable request.

Declarations

Ethics approval and consent to participate

Not applicable.

Consent for publication

Not applicable.

Competing interests

The authors declare no competing interests.

Received: 10 June 2025 / Accepted: 30 October 2025

Published online: 31 December 2025

References

1. Verma AK. in Introd. To Mod. Planar Transm. Lines Phys. Anal. Circuit Model. Approach, IEEE, 2021. 639–696. https://doi.org/10.1002/9781119632443.ch18.
2. Royo I, Fernández-García R, Gil I. Microwave resonators for wearable sensors design: a systematic review. Sensors. 2023;23:9103. https://doi.org/10.3390/s23229103.
3. Bogner A, et al. Planar microstrip ring resonators for microwave-based gas sensing: design aspects and initial transducers for humidity and ammonia sensing. Sensors. 2017;17:2422. https://doi.org/10.3390/s17102422.
4. Silalahi HM, Chiang Y-C, Huang C-Y. Fin interdigital capacitors. Sens Actuators A Phys. 2025;386:116347.
5. Pendry JB, Holden AJ, Robbins DJ, Stewart WJ. Magnetism from conductors and enhanced nonlinear phenomena. IEEE Trans Microw Theory Tech. 1999;47:2075–84.
6. Zhou J, Koschny T, Soukoulis CM. Magnetic and electric excitations in split ring resonators. Opt Express. 2007;15:17881–90.
7. Warsi ZH et al. Sensors for Structural Health Monitoring: A Review. In 2019 Second Int. Conf. Latest trends Electr. Eng. Comput. Technol. 2019; 1–6. https://doi.org/10.1109/INTELLECT47034.2019.8955453.
8. Senesky D .G., Jamshidi B.MEMS Strain Sensors for Intelligent Structural Systems BT In: Mukhopadhyay S.C. (eds). New Developments in Sensing Technology for Structural Health Monitoring. Springer Berlin Heidelberg. 2011; 63–74. https://doi.org/10.1007/978-3-642-21099-0_4
9. Alahnomi RA, et al. Review of recent microwave planar resonator-based sensors: techniques of complex permittivity extraction, applications, open challenges and future research directions. Sensors. 2021;21:2267. https://doi.org/10.3390/s21072267.

10. Schueler M, Mandel C, Puentes M, Jakoby R. Metamaterial inspired microwave sensors. IEEE Microwave Mag. 2012;13:57–68.
11. Chanv B, Bakhru S, Mehta V. Structural health monitoring system using IOT and wireless technologies. In 2017 Int. Conf. Intell. Commun. Comput. Tech. 2017; 151–157. https://doi.org/10.1109/INTELCCT.2017.8324036.
12. Prakash V, et al. Structural health monitoring of concrete bridges through artificial intelligence: a narrative review. Appl Sci. 2025;15:2025. https://doi.org/10.3390/app15094855.
13. Zhu L, et al. Structural deformation monitoring of flight vehicles based on optical fiber sensing technology: a review and future perspectives. Engineering. 2022;16:39–55.
14. Murthy NM, Kakade PD. Review on strain monitoring of aircraft using optical fibre sensor. Int J Electron Telecommun. 2022;68:625–34.
15. Ekinci G, Yalcinkaya AD, Dundar G, Torun H. Split-ring resonator-based strain sensor on flexible substrates for glaucoma detection. J Phys Conf Ser. 2016;757:12019.
16. Chu M, et al. Respiration rate and volume measurements using wearable strain sensors. NPJ Digit Med. 2019;2:8.
17. Kebe M, et al. Human vital signs detection methods and potential using radars: a review. Sensors. 2020;20:1454. https://doi.org/10.3390/s20051454.
18. Pan W, et al. Stretchable strain sensor for human motion monitoring based on an intertwined-coil configuration. Nanomaterials. 2020;10:1980.
19. Zhao S, Liu D, Yan F. Wearable resistive-type stretchable strain sensors: materials and applications. Adv Mater. 2025;37:2413929.
20. Lv Z, Li Y. Wearable sensors for vital signs measurement: a survey. J Sens Actuator Networks. 2022;11:19. https://doi.org/10.3390/jsan11010019.
21. Sonil NI, Ullah Z, Chen J, Wang GP. Wearable strain sensors for human motion detection and health monitoring based on hybrid graphite-textile flexible electrodes. J Mater Res Technol. 2023;26:764–74.
22. Viskadourakis Z, et al. Fabrication of mm-scale complementary split ring resonators, for potential application as water pollution sensors. Materials. 2023;16:5290.
23. Salim A, Ghosh S, Lim S. Low-cost and lightweight 3D-printed split-ring resonator for chemical sensing applications. Sensors. 2018;18:3049.
24. Liu X, Wei Y, Qiu Y. Advanced flexible skin-like pressure and strain sensors for human health monitoring. Micromachines. 2021;12:695. https://doi.org/10.3390/mi12060695.
25. Glisic B. Concise historic overview of strain sensors used in the monitoring of civil structures: the first one hundred years. Sensors. 2022;22:2397. https://doi.org/10.3390/s22062397.
26. Zymelka D, Togashi K, Kobayashi T. Concentric array of printed strain sensors for structural health monitoring. Sensors. 2020;20:1997. https://doi.org/10.3390/s20071997.
27. Lynch JP. An overview of wireless structural health monitoring for civil structures. Philos Trans R Soc Lond A Math Phys Eng Sci. 2006;365:345–72.
28. Salim A, Naqvi AH, Park E, Pham AD, Lim S. Inkjet printed kirigami inspired split ring resonator for disposable, low cost strain sensor applications. Smart Mater Struct. 2020;29:15016.
29. Chen X, et al. 3D printed high-performance spider web-like flexible strain sensors with directional strain recognition based on conductive polymer composites. Mater Lett. 2022;306:130935.
30. Eom S, Lim S. Stretchable complementary split ring resonator (CSRR)-based radio frequency (RF) sensor for strain direction and level detection. Sensors. 2016;16:1667. https://doi.org/10.3390/s16101667.
31. Tasolamprou AC, et al. Flexible 3D printed conductive metamaterial units for electromagnetic applications in microwaves. Materials (Basel). 2020;13:3879.
32. Ishikawa A, Kato T, Takeyasu N, Fujimori K, Tsuruta K. Selective electroless plating of 3D-printed plastic structures for three-dimensional microwave metamaterials. Appl Phys Lett. 2017;111:183102.
33. Viskadourakis Z, et al. 3D-printed metasurface units for potential energy harvesting applications at the 2.4 GHz frequency band. Crystals. 2021;11:1089. https://doi.org/10.3390/cryst11091089.
34. Melik R, Unal E, Perkgoz NK, Puttlitz C, Demir HV. Metamaterial-based wireless strain sensors. Appl Phys Lett. 2009;95:11106.
35. Wang B, Li Y, Gu T. Design of a metamaterial chipless RFID sensor tag for high temperature. AIP Adv. 2023;13:35218.
36. Pramanik B et al. Experimental study on permittivity of acrylic dielectric elastomer. In 2012 IEEE 10th Int. Conf. Prop. Appl. Dielectr. Mater. 2012; 1–4. https://doi.org/10.1109/ICPADM.2012.6319032.
37. Forge S, Vu K. Forming a 5G strategy for developing countries: a note for policy makers. Telecomm Policy. 2020;44:101975.
38. Shi J, et al. A 3D-printed flexible radio frequency strain sensor based on complementary split ring resonator. IEEE Sens J. 2023;23:4405–12.
39. Baghelani M, Abbasi Z, Daneshmand M. High-dynamic-range chipless microwave resonator-based strain sensor. IEEE Trans Instrum Meas. 2021;70:1–7.
40. Schossmann A, Bergmann A. Millimeter-wave metamaterial-based strain sensor concept. IEEE Sens J. 2024;24:15900–8.
41. Jia P, Zheng X, Zhou J. Dynamic variation of the dielectric permittivity of elastomers with mechanical constraints. AIP Adv. 2023;13:125007.
42. Jean-Mistral C, Sylvestre A, Basrour S, Chaillout J-J. Dielectric properties of polyacrylate thick films used in sensors and actuators. Smart Mater Struct. 2010;19:75019.
43. Tröls A, et al. Stretch dependence of the electrical breakdown strength and dielectric constant of dielectric elastomers. Smart Mater Struct. 2013;22:104012.
44. Sheng J, Chen H, Li B, Chang L. Temperature dependence of the dielectric constant of acrylic dielectric elastomer. Appl Phys A. 2013;110:511–5.
45. Choi D-S, Lee S-H, Kim S-Y. Transparent and soft haptic actuator for interaction with flexible/deformable devices. IEEE Access. 2020;8:170853–61.
46. Mahmoodi M, Donnell KM. Two-Dimensional In-Plane Strain FSS-Based Sensor. In 2022 IEEE Int. Symp. Antennas Propag. Usn. Radio Sci. Meet. 2022; 1256–1257. https://doi.org/10.1109/AP-S/USNC-URSI47032.2022.9886550.
47. Mahmoud HA, Nesser H, Mostafa TM, Ahmed S, Lubineau G. A fully printable strain sensor enabling highly-sensitive wireless near-field interrogation. Adv Sci. 2025;12:2411346.

48. Teng L, et al. Soft radio-frequency identification sensors: wireless long-range strain sensors using radio-frequency identification. Soft Robot. 2018;6:82–94.
49. Rodini S, Genovesi S, Manara G, Costa F. Chipless wireless strain sensor based on stretchable piezoresistive materials. IEEE Sens J. 2023;23:28912–22.
50. Yu H, Song L, Xiao C-Y-K, Peng M-G. Multilayer perceptron algorithm-enabled flexible laser-induced graphene microwave sensor for intelligent biomechanical monitoring of sedentary behaviors. Measurement. 2025;255:118084.
51. Wang X, et al. Flexible strain sensor based on a frequency selective surface. Opt Express. 2023;31:8884–96.
52. Jang S-D, Kang B-W, Kim J. Frequency selective surface based passive wireless sensor for structural health monitoring. Smart Mater Struct. 2013;22:25002.
53. Yoo Y, Jeong H, Lim D, Lim S. Stretchable screen-printed metasurfaces for wireless strain sensing applications. Extrem Mech Lett. 2020;41:100998.
54. Abdolrazzaghi M, Daneshmand M. Multifunctional ultrahigh sensitive microwave planar sensor to monitor mechanical motion: rotation, displacement, and stretch. Sensors. 2020;20:1184. https://doi.org/10.3390/s20041184.
55. Praveen AP, Menon SK, Babu JS, Donelli M, Hariprasad MP. An auxetic based geometric tuning approach in microwave sensors for enhanced sensitivity in strain measurements. Measurement. 2025;253:117826.
56. Mc Gee K, Anandarajah P, Collins D. Proof of concept novel configurable chipless RFID strain sensor. Sensors. 2021;21:6224. https://doi.org/10.3390/s21186224.
57. Reyes-Vera E, et al. High-sensitivity strain sensing using a flexible microstrip antenna with metamaterial resonator. IEEE Sens J. 2025;25:647–54.
58. Fan X, Li Y, Chen S, Xing Y, Pan T. Mechanical terahertz modulation by skin-like ultrathin stretchable metasurface. Small. 2020;16:2002484.

Publisher's Note